Excited-state exchange interaction in NiO determined by high-resolution resonant inelastic x-ray scattering at the Ni $M_{2,3}$ edges

Chun-Yu Liu [1,2,*] Kari Ruotsalainen,[1] Karl Bauer [1] Régis Decker [1] Annette Pietzsch [1] and Alexander Föhlisch [1,2,†]

[1]*Institute for Methods and Instrumentation for Synchrotron Radiation Research (PS-ISRR), Helmholtz-Zentrum Berlin für Materialien und Energie GmbH (HZB), Albert-Einstein-Strasse 15, 12489 Berlin, Germany*

[2]*Institut für Physik und Astronomie, Universität Potsdam, Karl-Liebknecht-Strasse 24-25, 14476 Potsdam, Germany*

(Received 1 December 2021; revised 4 March 2022; accepted 19 May 2022; published 5 July 2022)

The electronic and magnetic excitations of bulk NiO have been determined using the $^3A_{2g}$ to $^3T_{2g}$ crystal-field transition at the Ni $M_{2,3}$ edges with resonant inelastic x-ray scattering at 66.3- and 67.9-eV photon energies and 33-meV spectral resolution. Unambiguous assignment of the high-energy side of this state to a spin-flip satellite is achieved. We extract an effective exchange field of 89 ± 4 meV in the $^3T_{2g}$ excited final state from empirical two-peak spin-flip model. The experimental data is found consistent with crystal-field model calculations using exchange fields of 60–100 meV. Full agreement with crystal-field multiplet calculations is achieved for the incident photon energy dependence of line shapes. The lower exchange parameter in the excited state as compared to the ground-state value of 120 meV is discussed in terms of the modification of the orbital occupancy (electronic effects) and of the structural dynamics: (A) With pure electronic effects, the lower exchange energy is attributed to the reduction in effective hopping integral. (B) With no electronic effects, we use the $S = 1$ Heisenberg model of antiferromagnetism to derive a second-nearest-neighbor exchange constant $J_2 = 14.8 \pm 0.6$ meV. Based on the linear correlation between J_2 and the lattice parameter from pressure-dependent experiments, an upper limit of 2% local Ni-O bond elongation during the femtosecond scattering duration is derived.

DOI: 10.1103/PhysRevB.106.035104

I. INTRODUCTION

To establish the intrinsic electronic properties and their behavior upon excitation in strongly correlated systems is pivotal to link complex many-body physics to functionality. It is the interaction among orbital, charge, spin, and lattice degrees of freedom that gives rise to the development of quantum materials [1–4], and their applications range from electronic devices [5] to catalysts [6,7] and superconductors [8]. Scientists have developed their understanding and first-principles description of strongly correlated solids on the puzzling properties of NiO, serving as the paradigmatic strongly correlated antiferromagnetic (AFM) insulator [9]. NiO has a slightly distorted cubic rocksalt structure [10] with a Ni-O equilibrium bond length (R_e) of 2.09 Å at the ground state [11]. Locally, the Ni^{2+} center has sixfold coordination to 6 O^{2-} in octahedral (O_h) symmetry. In this local picture, the $3d$ states of the Ni ions are split by the crystal field, creating a $^3A_2$ ($S = 1$) ground state of the Ni atom. Driven by the (super-)exchange interaction, below the Néel temperature of 523 K, the spins arrange ferromagnetically (FM) on the (111) Ni-planes with AFM between the planes along the [111] direction [Fig. 1(a)]. This electronic structure and the concomitant local and long-range order parameters give rise to electronic, spin, and lattice excitations, charge transfer between the Ni $3d$ and the O $2p$ as well as emergent quasiparticle excitations, such as magnons.

A powerful probe to the rich low-energy magnetic excitation of NiO is inelastic neutron scattering (INS) [12], probing spin excitations with unrivaled energy resolution and wide range of momentum transfer across the Brillouin zone. RIXS has emerged also as a powerful probe for element-specific charge, orbital, spin, and lattice excitations and their emergent quasiparticles with high polarization control starting at the Brillouin zone center [13]. Other complementary spectroscopic techniques to probe crystal-field excitations in NiO are nonresonant inelastic x-ray scattering [14], UV-visible [15], spectroscopic ellipsometry [16], and electron energy-loss spectroscopy [17].

RIXS is a coherent second-order optical process that probes matter in a highly selective manner via the creation of a spin-polarized core-hole intermediate state [18]. Figure 1(b) shows schematically the states involved in the M-edge RIXS process for NiO. A $3p$-core electron is resonantly promoted via a dipole transition with linearly polarized radiation into unoccupied states, creating the spin-orbit split $3p_{3/2}$ and $3p_{1/2}$ core-excited states. Their natural core-hole lifetimes allow for ultrafast dynamics during the scattering duration time with the subsequent RIXS radiative decay channel, leading to low-energy excited states accompanying the resonant elastic-scattering channel back to the ground state. In particular, the core-excited intermediate states of the RIXS process are

*chun-yu.liu@helmholtz-berlin.de
†alexander.foehlisch@helmholtz-berlin.de

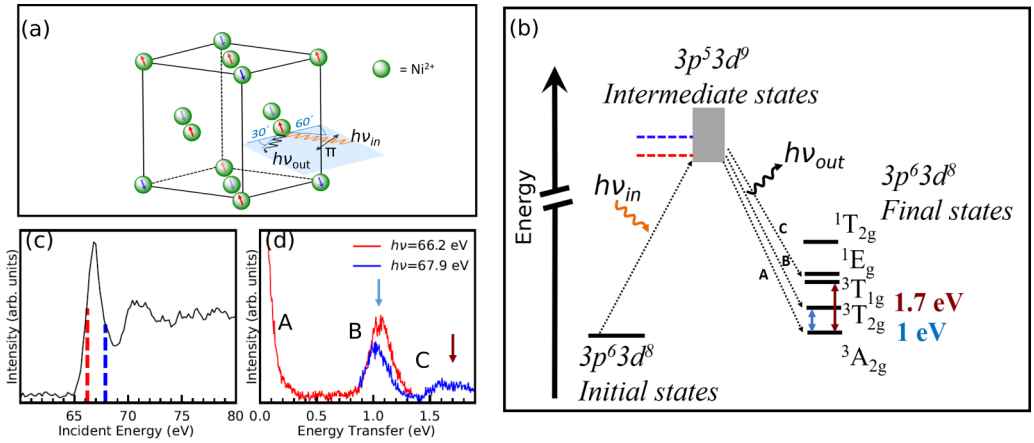

FIG. 1. (a) Experimental geometry used in M-edge x-ray absorption spectroscopy (XAS) and resonant inelastic x-ray scattering (RIXS). The arrows depict the orientation of the AFM-coupled magnetic moments. (b) Schematic RIXS process in NiO. The overlapping M-edge multiplets of the Ni $3p_{3/2}$ and Ni $3p_{1/2}$ core-excited intermediate states are shown as the gray band. The two RIXS photon energies across the M-edge absorption resonance are indicated with red and blue dashed lines connecting to the XAS spectrum in panel (c). A selection of the low-energy excited final states in RIXS relevant for M-edge RIXS is shown without the additional higher-energy crystal-field states. (c) XAS spectrum in total-fluorescence-yield mode with the two RIXS photon energies in red and blue dashed lines. (d) Experimental M-edge RIXS spectra.

crucial for spin-flip excitations. Creation of spin-orbit coupled core holes of defined total angular momentum j ($3p_{3/2}$ and $3p_{1/2}$ at the Ni-M edge) implies that spin s is not a good quantum number of the core-excited states alone, and RIXS across these resonances is accompanied with high probability by spin-flip excitation pathways.

The first implementation of the local spin-flip excitation into the crystal-field multiplet model describing RIXS was established by de Groot *et al.* [19], and the model serves since then as standard interpretation. The observables can be further broken down by using a Heisenberg model and the nearest-neighbor FM coupling of $J_1 \approx -1$ meV and next-to-nearest-neighbor AFM coupling of $J_2 \approx 19$ meV [20]. This approach has been successfully applied to interpret RIXS measurements at the Ni L_3 edge and to extract the exchange constant from the magnon dispersion relation [21]. Single and double magnon modes were also determined with high-resolution RIXS [21–24]. However, for Ni M-edge RIXS due to the strong diffuse scattering, limited instrumental resolution and low intensity, spin-flip excitations around ground state were obscured by the elastic peak tailing [25].

Probing the crystal-field excitations with M-edge RIXS is essential to better understand the electronic properties of strongly correlated materials since it delivers an alternative dynamic context due to the different scattering time defined by the core-hole lifetime. The different intermediate states also change the spectral weight in the final states. Therefore, new information can be revealed by utilizing different thresholds.

In this article, we report unprecedented high-resolution RIXS experiments at the Ni M edge to unambiguously determine the energy of local spin-flip excitations and related exchange parameters as well as the full set of crystal-field parameters. By combining our experimental results with crystal-field multiplet theory simulations, we find evidence for a local expansion of the lattice, which occurs upon the femtosecond excited-state lifetime.

II. EXPERIMENT

The M-edge RIXS experiments and supporting x-ray absorption XAS experiments were performed at BESSY II (HZB Berlin) at the beamline UE112-PGM1 with the meV-RIXS permanent end station [26]. A commercial (MaTecK) polished NiO (100) single crystal with 10-nm surface roughness and an orientational accuracy of $<2^\circ$ was investigated. The incident photon energy was calibrated with a helium gas cell where the $2,1_4$ resonance at 64.138 eV was set as the reference [27]. The measurements were carried out at room temperature at 10^{-8}-mbar pressure with a linearly horizontally polarized beam.

Figure 1 depicts the experimental geometry [Fig. 1(a)] and the schematics of relevant states involved in the Ni-M-edge RIXS process [Fig. 1(b)] in relation to the experimental Ni-M-edge RIXS results [Fig. 1(d)] obtained for the two photon energies 66.2 eV (red) and 67.9 eV (blue) across the Ni-M-edge x-ray absorption resonance [Fig. 1(c)]. Measurements were conducted with the incident beam at 30° to the sample normal at a fixed scattering angle of 90° on the horizontal plane. XAS was recorded in total fluorescence yield mode (FY), operating the RIXS spectrometer in 0th order scanning the incident photon energy by 0.2-eV steps from 60 to 80 eV. Overall beamline and spectrometer resolution was ≈33 meV at these excitation energies. Each RIXS spectrum has 3–8-h data-aquisition time.

Overall the high-resolution spectral features we recorded allow assignment of the established XAS and RIXS features described by previous work [25]. Distinct XAS features in Fig. 1(c) are the leading edge at 67 eV followed by the peak at 71 eV previously assigned to the strong multiplet effects rather than the $M_{2,3}$ spin-orbit coupling [19,25,28,29]. For RIXS in Fig. 1(d), we follow the established notation: (A) is the elastic peak consisting of nonresonant scattering and resonant elastic scattering back to the $^3A_{2g}$ ground state.

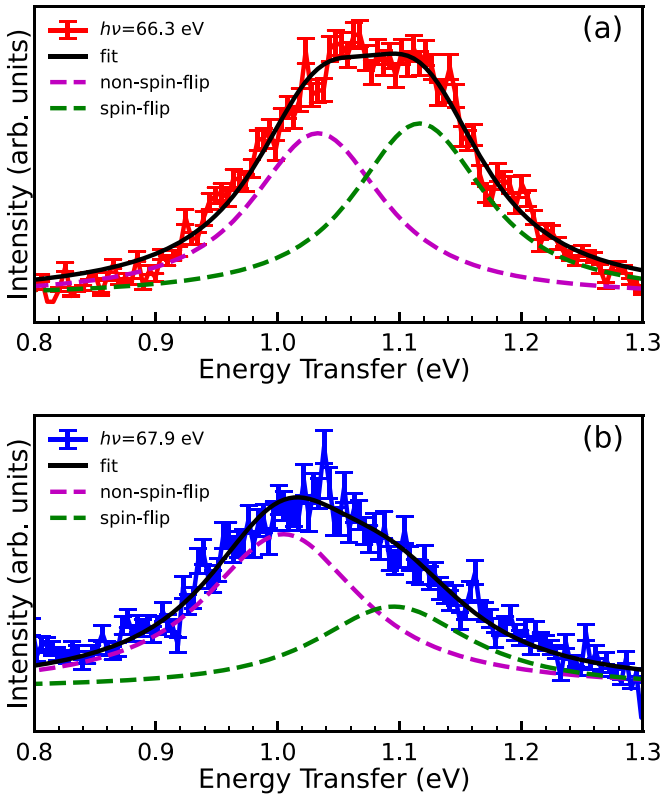

FIG. 2. Decomposition of the $^3A_{2g}$ to $^3T_{2g}$ d-d excitation observed by Ni M-edge RIXS channels in the empirical two-peak spin-flip model (without spin flip: purple dashed curve, spin flipped: green dashed curve). Scattered incident photon energy (a) $h\nu$ = 66.3 eV, (b) $h\nu$ = 67.9 eV. See the text for the fitting parameters, error bars, and constraints.

(B) is the $^3T_{2g}$ crystal-field excitation [15,30,31]. (C) is the $^3T_{1g}/^1E_g$ crystal-field excitation [32]. A constant dark-count background was subtracted in the RIXS spectra, and the signal intensity ratio between elastic and inelastic peaks (A:B) is ≈600:1.

III. RESULTS AND DISCUSSION

A. Two-peak spin-flip analysis

In Fig. 2 we show and analyze the fine structure of the crystal-field excitations within peak B for two chosen RIXS excitation energies 66.3 and 67.9 eV. As the first step, we assume the flipped and unflipped spin configurations motivate an empirical two-peak model of two Voigt functions with the Gaussian width fixed to the experimental resolution (33 meV, Supplemental Material Fig. S1) and the Lorentzian components constrained equally for each incident energy. In this approach, the two peaks represent the $^3A_{2g}$ to $^3T_{2g}$ (purple dashed curve) and the spin-flipped (green dashed curve) RIXS channels with peak distance and intensity to be determined from the experiments. For $h\nu$ = 66.3 eV [Fig. 2(a)] the peak separation is 88.8 ±4.6 meV at a Lorentzian broadening of 121 ±8-meV FWHM, based on the average intensity ratios and peak positions in our three independent measurements (Supplemental Material Figs. S2 and S3 [33]). For $h\nu$ = 67.9 eV [Fig. 2(b)] a splitting of 89.2 ±3.5 meV at a Lorentzian broadening of 145 ±18-meV FWHM is found. Thus, we observe within error bar an equivalent energy splitting. Since the RIXS spectral signature under investigation conserves the bandwidth of the scattered radiation of 33 meV, the 3p natural lifetime broadening of 1.19 eV [34] does not play a role in the line shape. Thus, the contributions from Lorentzian broadening and their slight increase from $h\nu$ = 66.3 over $h\nu$ = 67.9 eV reflect the different weights of the underlying final states and their lifetimes. This broadening is also beyond the reported maximum 3d spin-orbit splitting both in experiment [35] and in theoretical calculation [36], whereas low-energy modes, such as phonons due to shake-up effects cannot be excluded. Coupling of phonon shakeups to electronic transitions, however, is considered mild at M-edge charge neutral final states [37,38] and the energy (largest phonon energy = 58 meV [21]) is of the wrong scale considering the evolution of the shoulder peak. Even though the possibility of multiphonon progression cannot be excluded, its presence is not obvious based on the experimental data, and we consider it to be minor to no contribution to the spectral weight.

B. Crystal-field multiplet analysis

Crystal-field multiplet theory calculations (CFTs) have proven to describe XAS and RIXS spectra of localized electron systems, such as NiO with good accuracy [24,25,39]. Briefly summarized, the model accounts for the valence shell, core-valence Coulomb interaction, spin-orbit interactions, and an interaction of the valence with a point charge array with the symmetry of the point group of the absorbing atomic site. Furthermore, a magnetic environment about the absorbing atom can be described using an effective magnetic field given by the expression $B = zJ/2$, where z is the coordination number (z = 6 for NiO) and J is the exchange coupling. The ground-state electronic problem is solved with exact diagonalization. Spectral simulations are then performed using first-order perturbation theory for XAS and the Kramers-Heisenberg formula for RIXS. See Ref. [40] for the equations and implementation of CFT in the EDRIXS code used to produce the results presented here. We present the essential results in Figs. 3(a)–3(d).

The CFT calculations were performed for the RIXS spectra of the Ni^{2+} ion in O_h symmetry. The ground- and final-state intra-d-shell Coulomb interaction parameters were F^2_{dd} = 12.234 and F^4_{dd} = 7.598 eV. The intermediate-state core-valence interaction parameters were F^2_{pd} = 13.632, G^1_{pd} = 16.900, and G^3_{pd} = 10.277 eV. The 3d and 3p spin-orbit coupling constants were ζ_d = 0.083 and ζ_p = 1.2 eV. Following prior works, all Coulomb integrals were scaled to 70% of the bare Hartree-Fock values [25]. The crystal-field splitting 10 Dq was set to 1.07 eV by comparison with experiment at 66.3 eV. Finite temperature effects were considered by simulating the XAS and RIXS spectra for an ensemble of initial states with weights calculated from the Boltzmann distribution at 300 K.

The experimental fluorescence yield presented in Fig. 1(c) is compared to theory in Fig. 3(a). The experimental line shape is reproduced rather well in the region relevant to the

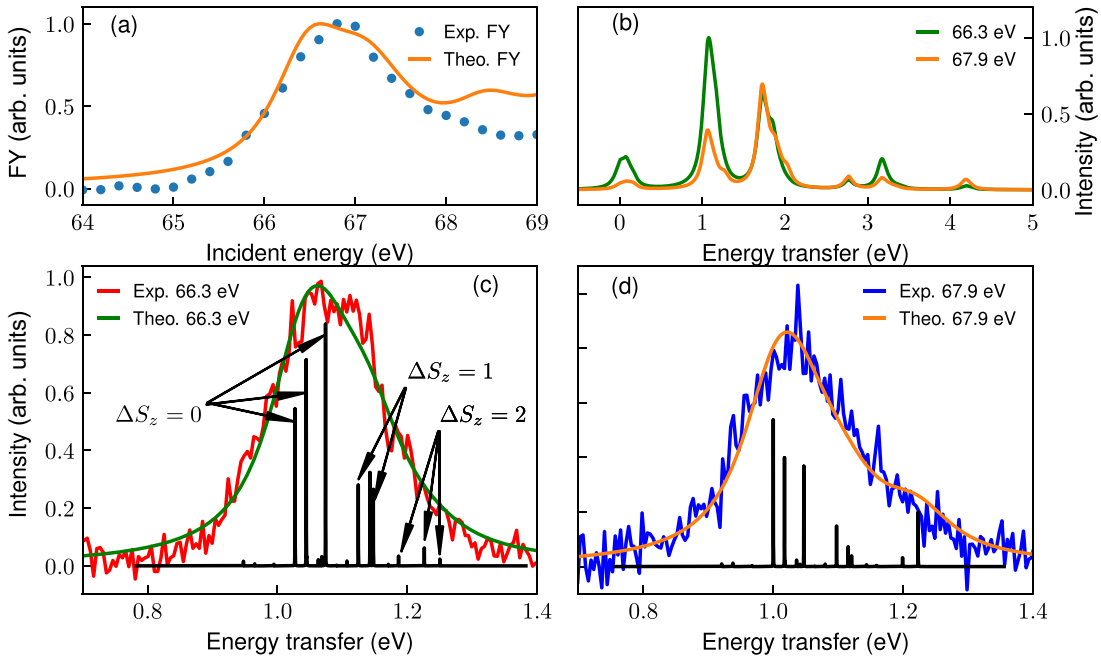

FIG. 3. (a) Experimental vs theoretical fluorescence yields. (b) The full RIXS spectra calculated at the experimental excitation energies. (c) A detailed view on the theoretical calculation for 66.3-eV excitation energy fitted to experiment as described in the text. The sticks represent the individual transitions. (d) The same as (c) for 67.9 eV.

subsequent RIXS calculations. The spin-orbit splitting at the $M_{2,3}$ edge is similar in magnitude as the multiplet, crystal-field splittings, and the core-hole lifetime broadening. Therefore, the intermediate states of the RIXS process are superpositions of several $3p^5 3d^9$ configurations [39]. The intermediate-state lifetime Γ for M-edge RIXS of transition metals is also known to vary considerably across the edge [37]. However this effect has a large impact only at higher excitation energies than considered here [37]. Thus, we used a fixed lifetime broadening of 1 eV full width at half maximum (FWHM).

The full RIXS spectra calculated for 66.3 and 67.9 eV excitation energies are presented in Fig. 3(b). The polarization vectors of the incident and scattered light were aligned to the crystal-field axes to reproduce the experimental geometry. The presented spectra are averages over vertical and horizontal outgoing polarization states. The RIXS spectrum for each polarization state is an average over the exchange field orientations applied to the spin in accordance with the AFM domain structure [24,41]. Here we show results obtained with an exchange splitting $E_{ex} = 80$ meV. A final-state lifetime broadening of 120-meV FWHM was used.

The structures near 0 eV energy loss in Fig. 3(b) correspond to spin-flip transitions within the ${}^3A_{2g}$ ground-state term. They correspond to $\Delta S_z = 1$ and $\Delta S_z = 2$ transitions with respect to the local ground-state spin orientation determined by the AFM coupling to next-to-nearest neighbor Ni ions. These transitions have recently been observed in a high-resolution L-edge RIXS experiment [24]. The ${}^3T_{2g}$ states are found near 1 eV followed by ${}^3T_{1g}/{}^1E_g$ below 2 eV. The positions of the states are in good agreement with the previous work in Ref. [25], but there are differences in the intensities. Their origin probably relates to the precise choice of the theoretical excitation energy and Coulomb interaction parameters.

Detailed comparisons to the experimental RIXS spectra of the ${}^3T_{2g}$ transition at 66.3- and 67.9-eV excitation energies are presented in Figs. 3(c) and 3(d), respectively. The black sticks mark the locations of the individual transitions contributing to the spectrum. The states contributing to the main and spin-flip transitions are marked with the black arrows in Fig. 3(c). Their energies are the same for Fig. 3(d). The weak side peaks originate from the small but finite population of the first excited state at 300 K. We note that the stick spectrum for 66.3 eV supports fitting the experiment with two peaks since the $\Delta S_z = 2$ lines contributes negligible intensity.

The ${}^3T_{2g}$ final state is split to nine sublevels in the presence of valence spin-orbit coupling and exchange splitting. To obtain information on the magnitude of the AFM exchange splitting, we performed CFT calculations using splittings of 60 to 140 meV in steps of 20 meV. The first group of three final states correspond to $\Delta S_z = 0$ transitions with respect to the ground state. The following two groups of three final states correspond to $\Delta S_z = 1$ and $\Delta S_z = 2$. It is important to note that the ΔS_z values were extracted from a separate calculation where the exchange field was applied perpendicular to the polarization vector of the incident light and are exact only in that case. A direct calculation showed that the final-state energies did not change when averaging over the AFM domain structure, but the intensities did vary as expected.

The calculated average transition intensities were then used to fit the experimental spectra with the following procedure: For each exchange splitting value, the intensity ratios of the transitions are fixed to the calculated values. The position of the first transition is allowed to vary, and the energy differences to the remaining transitions are fixed to the calculation. The transitions are represented with Voigt functions of 33-meV FWHM Gaussian part accounting for the experimental resolution and the Lorentzian final-state lifetime

broadening is assumed constant for all transitions and varied alongside the exchange splitting.

The outlined procedure was found to give results consistent with the experiment for an exchange splitting of 60–100 meV and final-state broadening of 100–140-meV FWHM. Overall the agreement is excellent, and the incident energy evolution of the RIXS line shape is well accounted for. We note that using the energy shift determined in Fig. 3(c) to fit Fig. 3(d) causes the agreement to worsen slightly. This is due to the first two $\Delta S_z = 0$ transitions being too intense in the calculation.

The physical origin of this is in the core-valence exchange interaction, i.e., in the precise values of G^1_{pd} and G^3_{pd}. Reducing the screening to 0.8 for G^1_{pd} and G^3_{pd} deemphasizes the transitions at the low-energy edge of the peak. After applying the final-state broadening, the essential effect of this is, however, an overall shift of the lines. The line shape itself is not affected in an essential way, justifying the adopted fitting procedure. We note that Ref. [24] also observed the sensitivity of the spin-flip transitions to the magnitudes of G^1_{pd} and G^3_{pd} but focused on the low-energy transitions.

We also found by direct calculation that the line shape was not changed appreciably by small variations on the order 0.1 eV in the excitation energy or the intermediate-state broadening, but they had more effect on the transition intensities. The approximation of constant final-state lifetime broadening on the other hand can have a considerable effect on the line shape. A calculation of the excited-state lifetimes taking strong electronic correlations and phonon-assisted decay of the final state is beyond the state of the art. The agreement with experiment is, nevertheless, convincing. Thus, we conclude that the presented comparison of crystal-field calculations and experiment support a reduction of the AFM exchange coupling from the ground-state value of 120 meV to the range of 60–100 meV in the $^3T_{2g}$ state.

C. Excited-state exchange interaction: electronic effects vs structural dynamics

At the $^3T_{2g}$ excited final state, the orbital occupations also change as holes are introduced into the t_{2g} states. This modifies the Ni-O hopping integrals, and to some extent the Coulomb interaction energy on the Ni site and the Ni-O charge transfer. All of which are parameters relevant to the interatomic exchange energy [42]. Therefore, a modification of the exchange energy due to the electronic configuration is expected when considering either the ground or the excited state. The t_{2g} hopping integral is roughly 60% of the e_g hopping in NiO [43]. We provide below an estimate of the magnitude of the electronic effect. Assuming that we have one e_g and one t_{2g} active electron in the final state, the effective hopping integral t reduces by a factor of $1/5$. As J is proportional to t^2, the excited-state value is reduced to $(4/5)^2$ or ≈64%, which is in line with the experimental result of reduced exchange energy. It would be interesting to see if thorough analytical or numerical calculations agree with the estimate provided here.

On the other hand, unlike INS which has no core-hole involved, previous L-edge experiments show systematically a smaller magnon energy near the $^3A_{2g}$ ground state [22,24] and, thus, with no modification of the electronic occupancy. This implies that core-excited-state-driven structural dynamics can be involved. A precise quantification of the contributions of electronic redistribution and nuclear dynamics is beyond the scope of this paper. The extracted excited-state exchange energy $E_{ex} = 89$ meV is to be considered representing a sum of the two effects. Below we discuss the limiting case of considering only lattice effects.

TABLE I. List of exchange energy and exchange constant from different measuring techniques. Different quanta magnons are abbreviated as M. The exchange constant J_2 is listed as reported with its according model. (2PSF: 2-peak spin-flip analysis and CFT).

Method	Exchange energy (meV)	J_2 (meV)
M-edge RIXS (this paper)	89 ±4 (2PSF)	14.8 ±0.6
	60–100 (CFT)	
Optical Raman	$2M \approx 194$ [44]	18.3 [44]
	$4M \approx 347$ [45]	
Electron tunneling	$2M \approx 186$ mV [46]	
Inelastic neutron scattering	≈114 [20]	19.01 [20]
M-edge RIXS	125 ±15 [25]	
Spectroscopic ellipsometry	≈100 [16]	
L-edge RIXS	≈105 [24]	
	95 [22]	
	≈100 [21]	18 [21]

By assuming no such electronic effects on the superexchange interaction, the exchange constants can be extracted from the intersite AFM interaction by applying the Heisenberg model. The underlying interaction is then parametrized with the interatomic exchange constants J_1 (nearest neighbor) and J_2 (second-nearest neighbor) [47,48]. For simplification, J_1 (≈ -1 meV), which is small compared to J_2 (≈ 19 meV) [20], is neglected and the exchange energy can be expressed as $E_{ex} = 6J_2$ [13,22,49].

In Table I, we compare our Ni M-edge RIXS empirically derived $J_2 = 14.8$-meV value to values extracted by other methods. In general, the single- and multimagnon energies from low-energy loss features are in good agreement with inelastic neutron scattering, optical Raman, ellipsometry, and electron tunneling. We note in this context that both the Ni M-edge and L-edge RIXS studies are trending to values on the lower side, e.g., Betto *et al.* observed lower magnon energies than INS near the zone boundary [21]. The L-edge RIXS result [24] probes the magnon energy close to the ground state and via a different core-excited intermediate state ($2p$ vs $3p$ core hole). We also note that the prior M-edge result [25] is the deviating case, and this is likely explained by the limitation in resolution. A possible underlying cause is the strong correlation between the local Ni-O bond length with the exchange constant [50,51]. Since the RIXS process involves a transient core-excited state, a structural force is exerted on the lattice during the scattering duration time. Thus, the d-d excited final state may have inherited a small structural distortion. In that sense, our experiments prove that the RIXS process gives access intrinsically to the effect of such distortions present during the excited state on the physical constants, such as the exchange constant. Based on the extrapolation of the correlation between J_2 and the lattice parameter [52], which is derived from pressure-dependent Raman experiments and

assuming no changes in the electronic properties in the excited states, we derive for the Ni M-edge measured $^3T_{2g}$ state of NiO a maximum limit ≈2% locally expanded average Ni-O distance of ≈ 2.13 Å over the ground-state equilibrium distance of 2.09 Å. It is also apparent that thermal expansion due to beam heating is not the main contribution since it requires a hypothetical increase of, at least, ≈2000 K to bring about the same magnitude of an effect [53]. This is three orders of magnitude above the absorbed energy from synchrotron radiation in the probed sample volume.

RIXS is a photon-scattering process which generally has a lifetime at the femtosecond scale defined by the core-hole lifetime. At the L_3 edge the core-hole lifetime of Ni is $\Gamma =$ 0.2–0.5 eV [54] whereas at the M_3 edge the value is $\Gamma =$ 1.19 eV [34]. In a periodic lattice, the ground-state core levels are equally symmetry adapted as the valence states. After x-ray absorption, dynamic relaxation sets in, leading to local symmetry reduction. The core-excited state reflects a balance of symmetry adapted, itinerant, and localized atomic impurity states, which are a superposition of various structural and vibronic excitations. This signature of dynamics during the scattering duration (core-hole lifetime) is captured in the RIXS spectral shape [18]. In addition, the d-d excited final state brings also a distortion with its even longer valence-hole lifetime, based on our empirical and theoretical models ($\Gamma =$ 0.12 eV). In sum, we, thus, attribute these dynamic localization aspects, together with the electronic redistribution to the lower $^3T_{2g}$ excited-state exchange energy.

IV. SUMMARY AND CONCLUSION

To summarize, nickel M-edge RIXS at NiO with energy resolution far below the intrinsic broadening mechanisms is a powerful tool to extract quantitative values for crucial electronic structure parameters in a functional oxide. The spin-flip satellite of the d-d excited $^3T_{2g}$ final state of a bulk single-crystal NiO has been observed. Full crystal-field theory calculations are in excellent agreement with the measured spectra in support of the given assignment with dominant $\Delta S_z = 0$ and $\Delta S_z = 1$ contributions. We extract an exchange energy of 89 meV and exchange constant $J_2 = 14.8$ meV. Compared to other probes, such as optical, L-edge x-ray, or inelastic neutron-scattering approaches, we observe a smaller exchange constant, which is attributed to contribution from both electronic effects and structural dynamics. With pure electronic effects, the estimate based on the reduction in the effective hopping integral delivers a reduction to ≈64% in exchange energy. With the assumption of no electronic effects, we derive an effective ≈2% local Ni-O bond elongation during the nickel M-edge scattering duration time.

[1] J. Varignon, M. N. Grisolia, J. Íñiguez, A. Barthélémy, and M. Bibes, npj Quantum Mater. **2**, 21 (2017).
[2] A. Mercy, J. Bieder, J. Íñiguez, and P. Ghosez, Nat. Commun. **8**, 1677 (2017).
[3] K. Haule and G. L. Pascut, Sci. Rep. **7**, 10375 (2017).
[4] C. Ahn, A. Cavalleri, A. Georges, S. Ismail-Beigi, A. J. Millis, and J. M. Triscone, Nat. Mater. **20**, 1462 (2021).
[5] J. Shi, S. D. Ha, Y. Zhou, F. Schoofs, and S. Ramanathan, Nat. Commun. **4**, 2676 (2013).
[6] P. Kalyani and N. Kalaiselvi, Sci. Technol. Adv. Mater. **6**, 689 (2005).
[7] X. Ma, J. S. Carneiro, X. K. Gu, H. Qin, H. Xin, K. Sun, and E. Nikolla, ACS Catal. **5**, 4013 (2015).
[8] A. Bussmann-Holder and H. Keller, Zeitschrift fur Naturforsch. - Sect. B J. Chem. Sci. **75**, 3 (2020).
[9] S. Hüfner, Adv. Phys. **43**, 183 (1994).
[10] H. P. Rooksby, Nature (London) **152**, 304 (1943).
[11] N. Rinaldi-Montes, P. Gorria, D. Martínez-Blanco, A. B. Fuertes, L. Fernández Barquín, J. Rodríguez Fernández, I. De Pedro, M. L. Fdez-Gubieda, J. Alonso, L. Olivi, G. Aquilanti, and J. A. Blanco, Nanoscale **6**, 457 (2014).
[12] Y.-J. Kim, A. P. Sorini, C. Stock, T. G. Perring, J. van den Brink, and T. P. Devereaux, Phys. Rev. B **84**, 085132 (2011).
[13] L. J. P. Ament, M. van Veenendaal, T. P. Devereaux, J. P. Hill, and J. van den Brink, Rev. Mod. Phys. **83**, 705 (2011).
[14] B. C. Larson, W. Ku, J. Z. Tischler, C.-C. Lee, O. D. Restrepo, A. G. Eguiluz, P. Zschack, and K. D. Finkelstein, Phys. Rev. Lett. **99**, 026401 (2007).
[15] R. Newman and R. M. Chrenko, Phys. Rev. **114**, 1507 (1959).
[16] T. D. Kang, H. S. Lee, and H. Lee, J. Korean Phys. Soc. **50**, 632 (2007).
[17] A. Gloter, M. W. Chu, M. Kociak, C. H. Chen, and C. Colliex, Ultramicroscopy **109**, 1333 (2009).
[18] F. Gel'mukhanov, M. Odelius, S. P. Polyutov, A. Föhlisch, and V. Kimberg, Rev. Mod. Phys. **93**, 035001 (2021).
[19] F. M. F. de Groot, P. Kuiper, and G. A. Sawatzky, Phys. Rev. B **57**, 14584 (1998).
[20] M. T. Hutchings and E. J. Samuelsen, Phys. Rev. B **6**, 3447 (1972).
[21] D. Betto, Y. Y. Peng, S. B. Porter, G. Berti, A. Calloni, G. Ghiringhelli, and N. B. Brookes, Phys. Rev. B **96**, 020409(R) (2017).
[22] G. Ghiringhelli, A. Piazzalunga, C. Dallera, T. Schmitt, V. N. Strocov, J. Schlappa, L. Patthey, X. Wang, H. Berger, and M. Grioni, Phys. Rev. Lett. **102**, 027401 (2009).
[23] C. Schulz, K. Lieutenant, J. Xiao, T. Hofmann, D. Wong, and K. Habicht, J. Synchrotron Radiat. **27**, 238 (2020).
[24] A. Nag, H. C. Robarts, F. Wenzel, J. Li, H. Elnaggar, R. P. Wang, A. C. Walters, M. García-Fernández, F. M. F. de Groot, M. W. Haverkort, and K. J. Zhou, Phys. Rev. Lett. **124**, 067202 (2020).
[25] S. G. Chiuzbăian, G. Ghiringhelli, C. Dallera, M. Grioni, P. Amann, X. Wang, L. Braicovich, and L. Patthey, Phys. Rev. Lett. **95**, 197402 (2005).
[26] K. Bauer, J.-S. Schmidt, F. Eggenstein, R. Decker, K. Ruotsalainen, A. Pietzsch, T. Blume, C.-Y. Liu, C. Weniger, F. Siewert, J. Buchheim, G. Gwalt, F. Senf, P. Bischoff, L. Schwarz, K. Effland, M. Mast, T. Zeschke, I. Rudolph, A.

Meißner, and A. Föhlisch, J. Synchrotron Radiat. **29**, 908 (2022).
[27] K. Schulz, G. Kaindl, M. Domke, J. D. Bozek, P. A. Heimann, A. S. Schlachter, and J. M. Rost, Phys. Rev. Lett. **77**, 3086 (1996).
[28] L. A. Wray, W. Yang, H. Eisaki, Z. Hussain, and Y. D. Chuang, Phys. Rev. B **86**, 195130 (2012).
[29] E. Augustin, H. He, L. Miao, Y. D. Chuang, Z. Hussain, and L. A. Wray, J. Electron Spectrosc. Relat. Phenom. **220**, 121 (2017).
[30] A. Kotani, M. Matsubara, T. Uozumi, G. Ghiringhelli, F. Fracassi, C. Dallera, A. Tagliaferri, N. B. Brookes, and L. Braicovich, Radiat. Phys. Chem. **75**, 1670 (2006).
[31] V. I. Sokolov, V. A. Pustovarov, V. N. Churmanov, V. Y. Ivanov, N. B. Gruzdev, P. S. Sokolov, A. N. Baranov, and A. S. Moskvin, JETP Lett. **95**, 528 (2012).
[32] M. Magnuson, S. M. Butorin, A. Agui, and J. Nordgren, J. Phys.: Condens. Matter **14**, 3669 (2002).
[33] See Supplemental Material at http://link.aps.org/supplemental/10.1103/PhysRevB.106.035104 for files that include the energy calibration and the according spectral resolution over the detector window, three replications of the two energies, and the experimental data at two incident energies.
[34] R. Nyholm, N. Martensson, A. Lebuglet, and U. Axelsson, J. Phys. F: Met. Phys. **11**, 1727 (1981).
[35] M. Fiebig, D. Fröhlich, T. Lottermoser, V. V. Pavlov, R. V. Pisarev, and H. J. Weber, Phys. Rev. Lett. **87**, 137202 (2001).
[36] K. Satitkovitchai, Y. Pavlyukh, and W. Hübner, Phys. Rev. B **72**, 045116 (2005).
[37] L. A. Wray, S.-W. Huang, I. Jarrige, K. Ikeuchi, K. Ishii, J. Li, Z. Q. Qiu, Z. Hussain, and Y.-D. Chuang, Front. Phys. **3**, 32 (2015).
[38] L. A. Wray, J. Li, Z. Q. Qiu, J. Wen, Z. Xu, G. Gu, S. W. Huang, E. Arenholz, W. Yang, Z. Hussain, and Y. D. Chuang, Phys. Rev. B **88**, 035105 (2013).
[39] L. A. Wray, S.-W. Huang, Y. Xia, M. Z. Hasan, C. Mathy, H. Eisaki, Z. Hussain, and Y.-D. Chuang, Phys. Rev. B **91**, 035131 (2015).
[40] Y. Wang, G. Fabbris, M. Dean, and G. Kotliar, Comput. Phys. Commun. **243**, 151 (2019).
[41] I. Sänger, V. V. Pavlov, M. Bayer, and M. Fiebig, Phys. Rev. B **74**, 144401 (2006).
[42] J. Zaanen and G. A. Sawatzky, Can. J. Phys. **65**, 1262 (1987).
[43] M. W. Haverkort, M. Zwierzycki, and O. K. Andersen, Phys. Rev. B **85**, 165113 (2012).
[44] R. E. Dietz, G. I. Parisot, and A. E. Meixner, J. Appl. Phys. **42**, 1484 (1971).
[45] R. E. Dietz, W. F. Brinkman, A. E. Meixner, and H. J. Guggenheim, Phys. Rev. Lett. **27**, 814 (1971).
[46] D. C. Tsui, R. E. Dietz, and L. R. Walker, Phys. Rev. Lett. **27**, 1729 (1971).
[47] Y. Yamamoto and T. Nagamiya, J. Phys. Soc. Jpn. **32**, 1248 (1972).
[48] D. Ködderitzsch, W. Hergert, W. M. Temmerman, Z. Szotek, A. Ernst, and H. Winter, Phys. Rev. B **66**, 064434 (2002).
[49] S. J. Joshua and F. D. Morgan, Phys. Status Solidi B **59**, 269 (1973).
[50] Y. Mita, Y. Ishida, M. Kobayashi, and S. Endo, J. Phys.: Condens. Matter **14**, 11173 (2002).
[51] E. Cazzanelli, A. Kuzmin, N. Mironova-Ulmane, and G. Mariotto, Phys. Rev. B **71**, 134415 (2005).
[52] M. J. Massey, N. H. Chen, J. W. Allen, and R. Merlin, Phys. Rev. B **42**, 8776 (1990).
[53] J. M. Keem and J. E., Honig, Selected electrical and thermal properties of undoped nickel oxide, CINDAS Report 52, West Lafayette, Indiana, USA, Technical Report, 1978 (unpublished).
[54] J. Campbell and T. Papp, At. Data Nucl. Data Tables **77**, 1 (2001).